PNAS

Supporting Information for

Facet-switching of rate-determining step on copper in CO_2-to-ethylene electroreduction

Yu-Cai Zhang[1†], Xiao-Long Zhang[1†], Zhi-Zheng Wu[1†], Zhuang-Zhuang Niu[1], Li-Ping Chi[1], Fei-Yue Gao[1], Peng-Peng Yang[1], Ye-Hua Wang[1], Peng-Cheng Yu[1], Jing-Wen Duanmu[1], Shu-Ping Sun[1], Min-Rui Gao[1*]

[1]Division of Nanomaterials & Chemistry, Hefei National Laboratory for Physical Sciences at the Microscale, Department of Chemistry, University of Science and Technology of China, Hefei 230026, China.

[†]These authors contributed equally to this work.

*Min-Rui Gao
Email: mgao@ustc.edu.cn

This PDF file includes:
       Supporting text
       Figures S1 to S27
       Tables S1 to S11
       SI References

Supporting Information Text

CO₂R product analysis. Gas-phase products were quantified by Trace-1300 gas chromatography. A thermal conductivity detector (TCD) and a flame ionization detector (FID) were used to quantify H_2, CO, and other alkane contents, respectively. The FE of the gas product was calculated by the following formula:

$$FE(\%)= \frac{nxFV}{j_{total}} \times 100\% \qquad \text{(Equation S1)}$$

Where x is the mole fraction of the product, n is the number of electrons transferred, V is the outlet gas flow rate, F is Faraday's constant and j_{total} is the total current.

^{1}H NMR was performed using water suppression mode on Bruker 400 MHz spectrometer in order to determine liquid phase products. The dimethyl sulfoxide (DMSO) with a concentration of 50 ppm was used as the internal standard. To ensure full relaxation and quantization, the same spectral acquisition parameters were used for all measurements. The FE of the liquid product was calculated by the following formula:

$$FE(\%)= \frac{Q_i}{Q_{total}} \times 100\% = \frac{nCVF}{It} \qquad \text{(Equation S2)}$$

where Q_{total} is the total amount of charge passing through the working electrode, Q_i is the amount of charge transferred for product i formation, C is the concentration of the liquid product in the catholyte measured by NMR, V is the volume of the catholyte, F is Faraday's constant, n is the electrons transferred for reduction to a molecule product, t is the electrochemical measurement time and I is the total current during electrolysis.

The half-cell power conversion efficiency (PCE) of C_2H_4 was calculated by the following formula:

$$PCE= \frac{(1.23-E_{C_2H_4}) \times FE_{C_2H_4}}{1.23-E} \times 100\% \qquad \text{(Equation S3)}$$

where E is the applied potential versus RHE, $E_{C_2H_4}$ is the thermodynamic potential versus RHE, $FE_{C_2H_4}$ is the FE of C_2H_4.

The energy efficiency (EE) of C_2H_4 was calculated by the following equation:

$$EE= \frac{E'_{C_2H_4}}{E'} \times FE_{C_2H_4} \qquad \text{(Equation S4)}$$

where E' is the cell voltage measured experimentally, $E'_{C_2H_4}$ represents the theoretical cell voltage from the thermodynamic calculation (1.15 V), $FE_{C_2H_4}$ is the FE of C_2H_4.
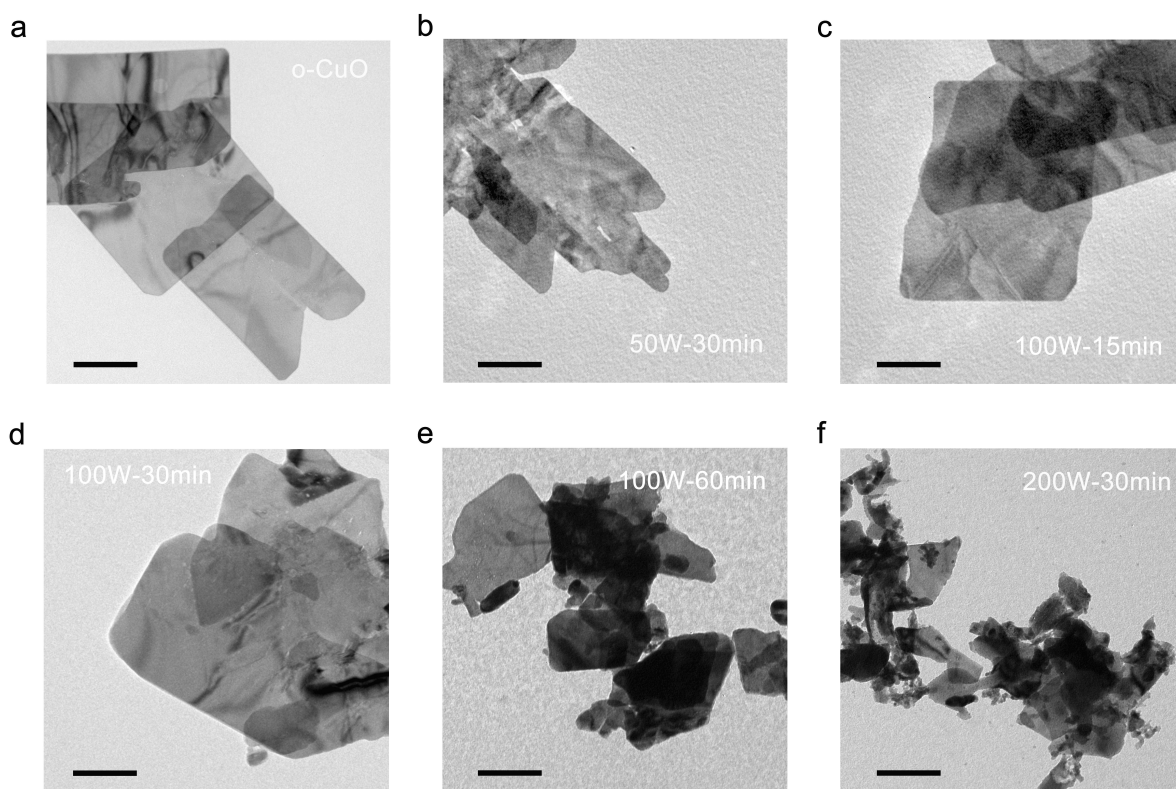
Fig. S1. Morphology characterization of the CuO catalysts. TEM images of o-CuO (a), 50W-30min (b), 100W-15min (c). 100W-30min (p-CuO) (d). 100W-60min (e) and 200W-30min (f). Scale bars, 200 nm. As the treatment power or time increases, the number of structural defects in the material gradually increases. By further increasing treatment power or time, the sheet structure was broken into irregular small fragments.
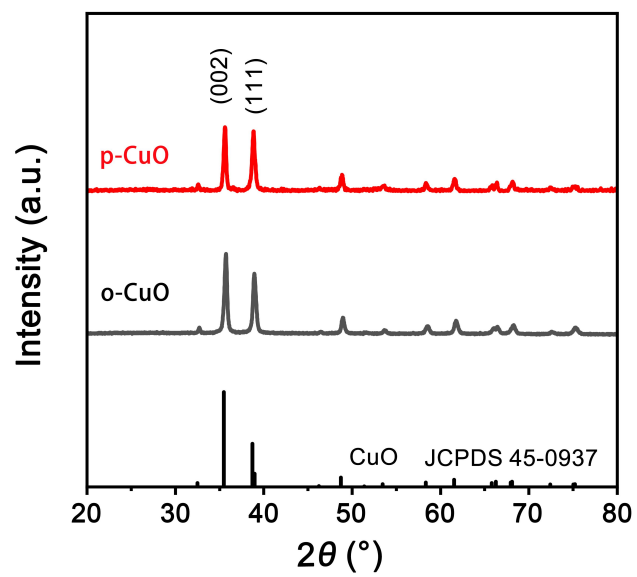
Fig. S2. XRD characterization. XRD patterns of o-CuO and p-CuO.
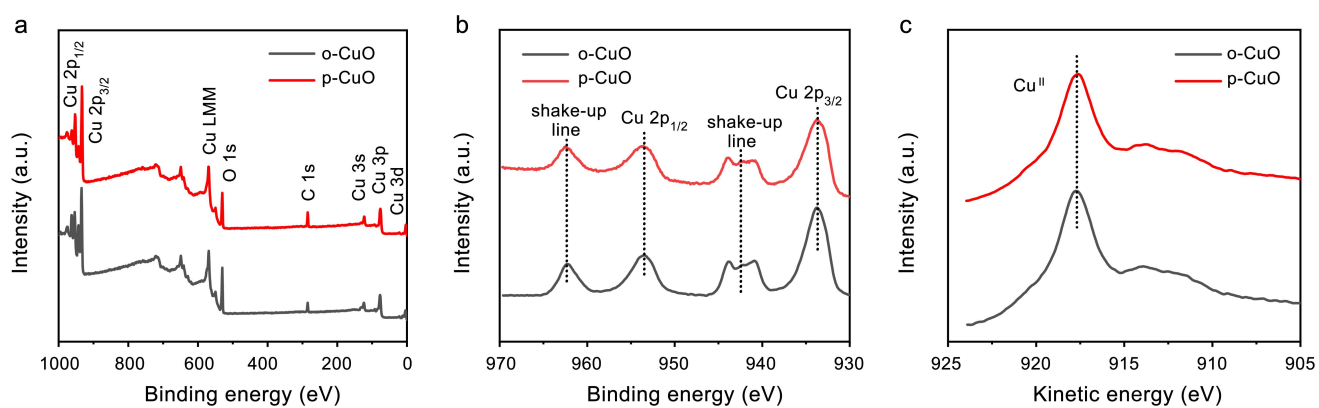
**Fig. S3.** XPS characterization of o-CuO and p-CuO. (a) The XPS survey spectra for o-CuO and p-CuO. (b) Cu 2p XPS spectra for o-CuO and p-CuO. The typical peaks at 933.7 and 953.6 eV correspond to the Cu $2P_{3/2}$ and Cu $2P_{1/2}$ of Cu^{2+}, respectively, as well as their concomitant shake-up lines at 942.3 eV and 962.4 eV. (c) Cu LMM spectra for o-CuO and p-CuO. The typical peaks at 917.7 eV correspond to the Cu^{2+}. (1)
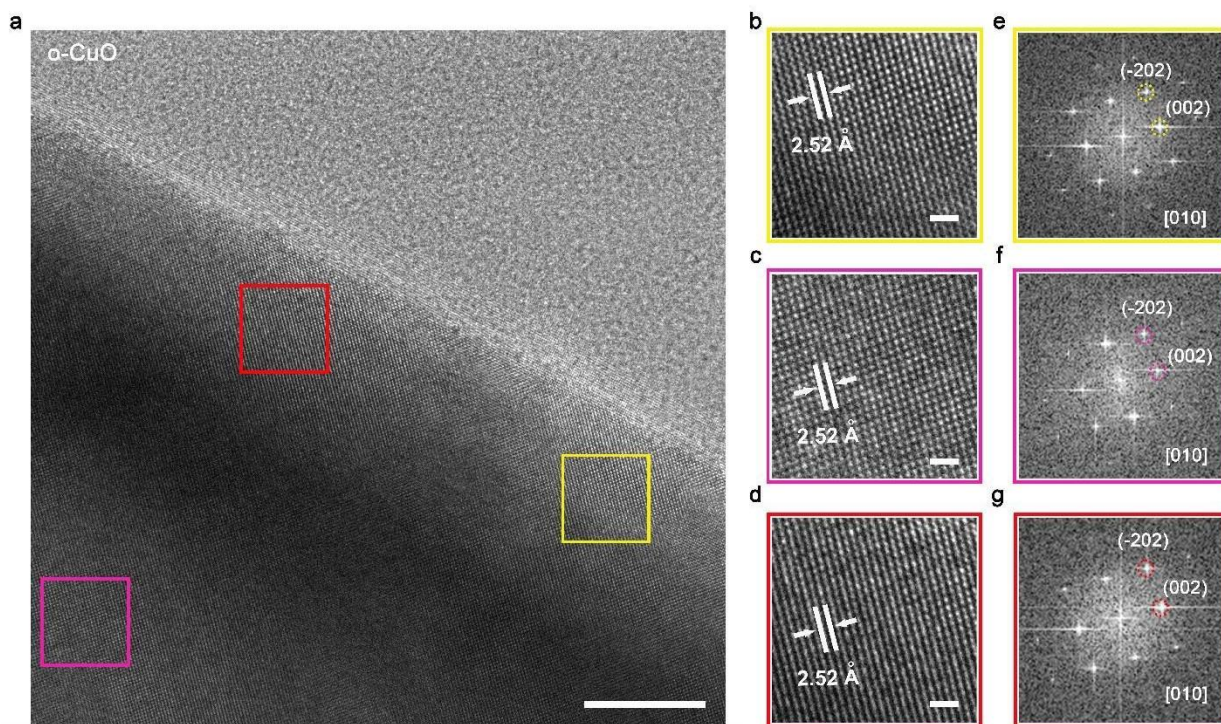
Fig. S4. Structural characterization of o-CuO. (a) HRTEM image of o-CuO. (b-d) Partially enlarged HRTEM image in the squares of (a). They were taken from randomly-selected spots. (e-g) Corresponding FFT patterns of (b-d), respectively. Scale bars, (a) 10 nm; (b-d) 1 nm.
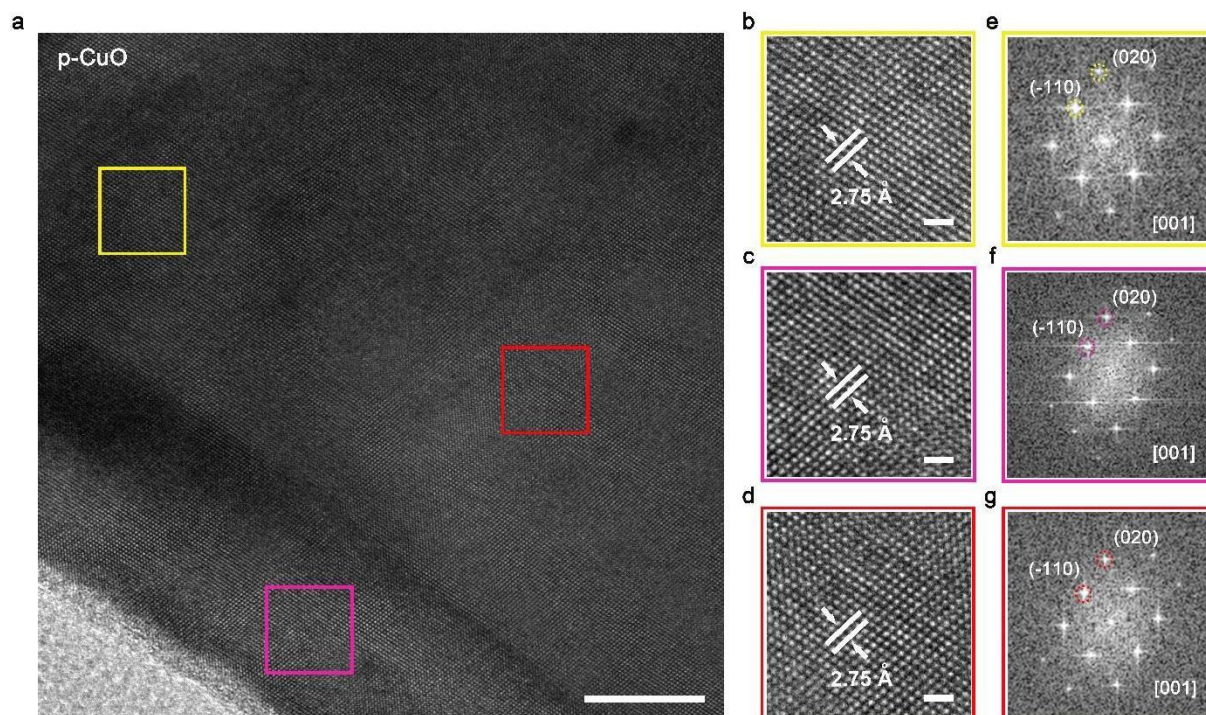
Fig. S5. Structural characterization of p-CuO. (a) HRTEM image of p-CuO. (b-d) Partially enlarged HRTEM image in the squares of (a). They were taken from randomly-selected spots. (e-g) Corresponding FFT patterns of (b-d), respectively. Scale bars, (a) 10 nm; (b-d) 1 nm.
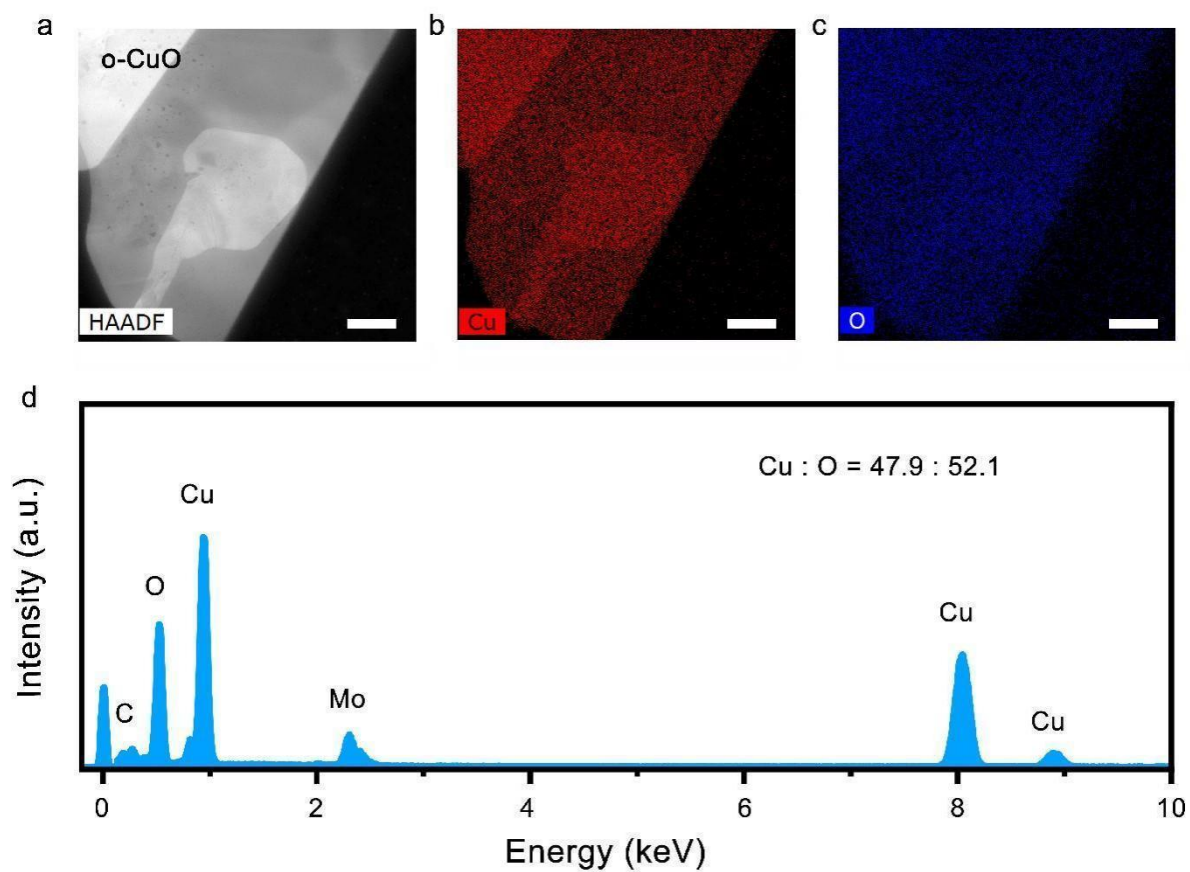
Fig. S6. Elemental analysis of o-CuO. (a-c) HAADF-STEM image (a) and EDS mapping (b, c) of o-CuO. The results revealed that Cu and O were uniformly distributed in the catalyst. Scale bar, 100 nm. (d) The proportion of elements in o-CuO. The ratio of Cu and O elements was close to 1:1.
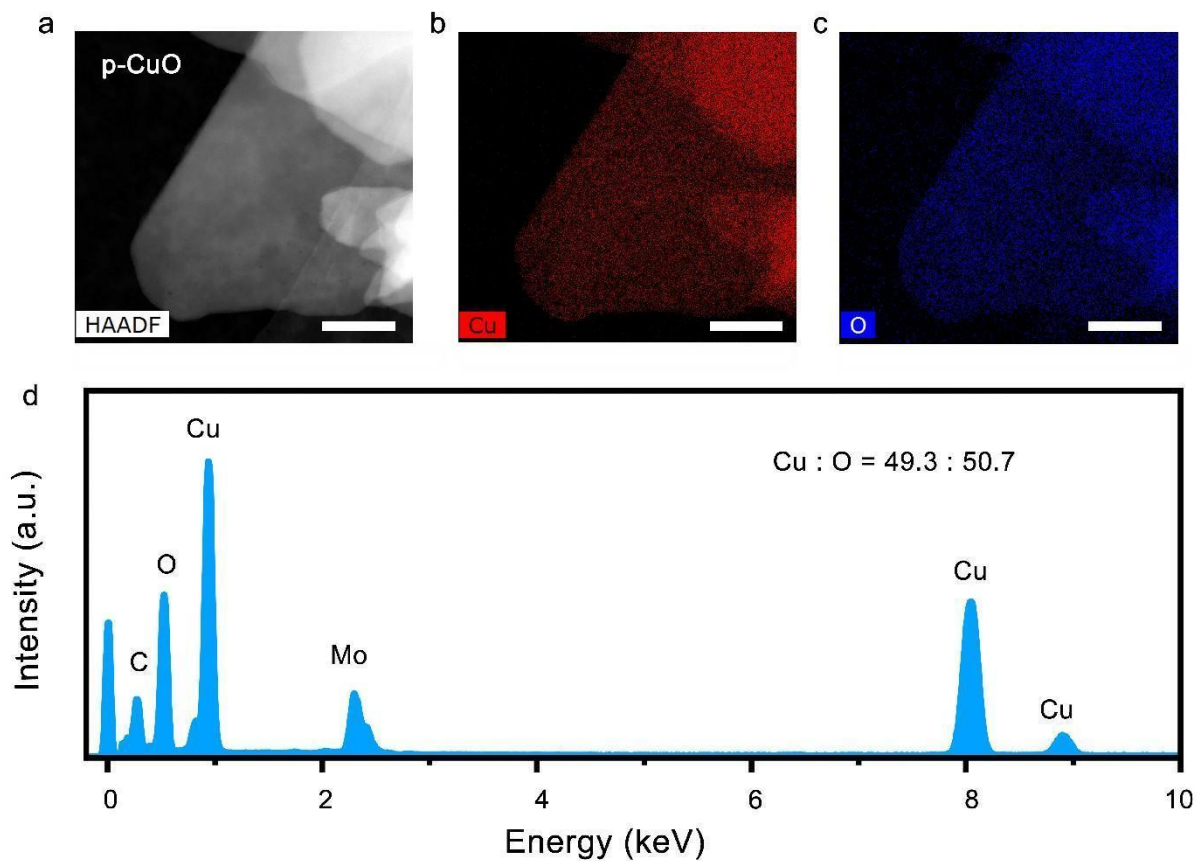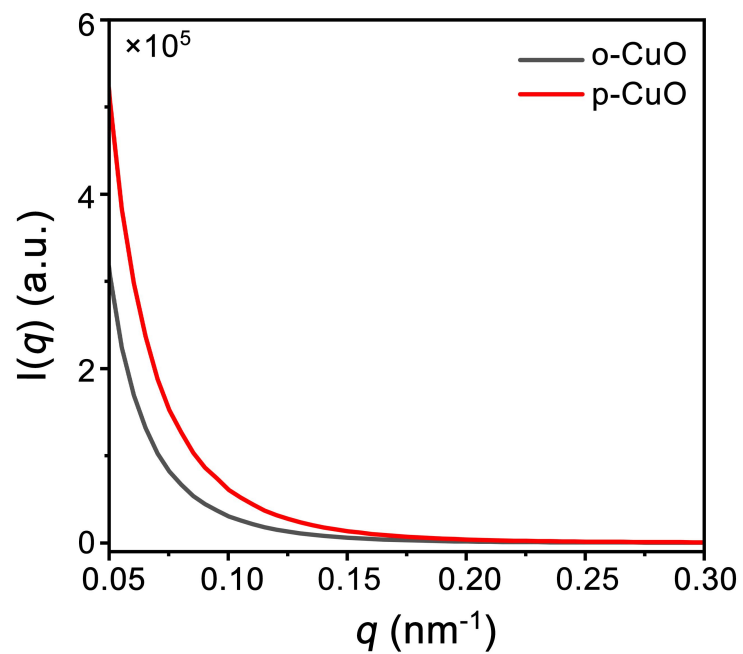
Fig. S7. Elemental analysis of p-CuO. (a-c) HAADF-STEM image (a) and EDS mapping (b, c) of p-CuO. The results revealed that Cu and O were uniformly distributed in the catalyst. Scale bar, 100 nm. (d) The proportion of elements in p-CuO. The ratio of Cu and O elements was close to 1:1.

Fig. S8. Small angle X-ray scattering (SAXS) studies of o-CuO and p-CuO. The 2-D SAXS images were obtained from the detector and transformed into the profiles of intensity (I) vs wavevector (q) by the software FiT2D.
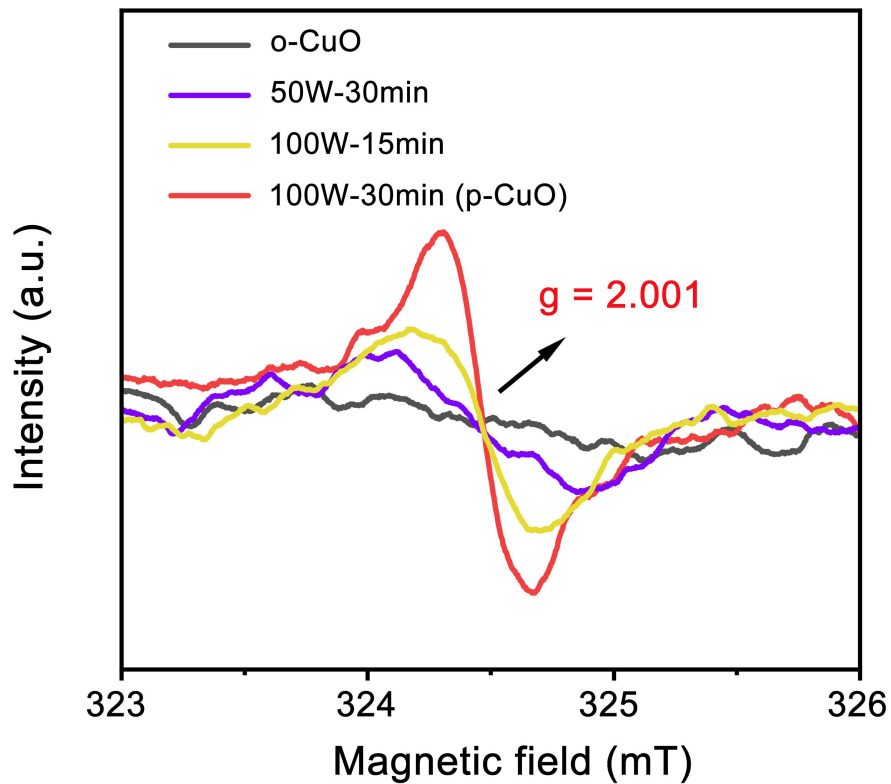
Fig. S9. EPR spectra of o-CuO and p-CuO. The characteristic waveform at g = 2.001 represented the formation of oxygen vacancies. (2) This proved the presence of defective oxygen in p-CuO.
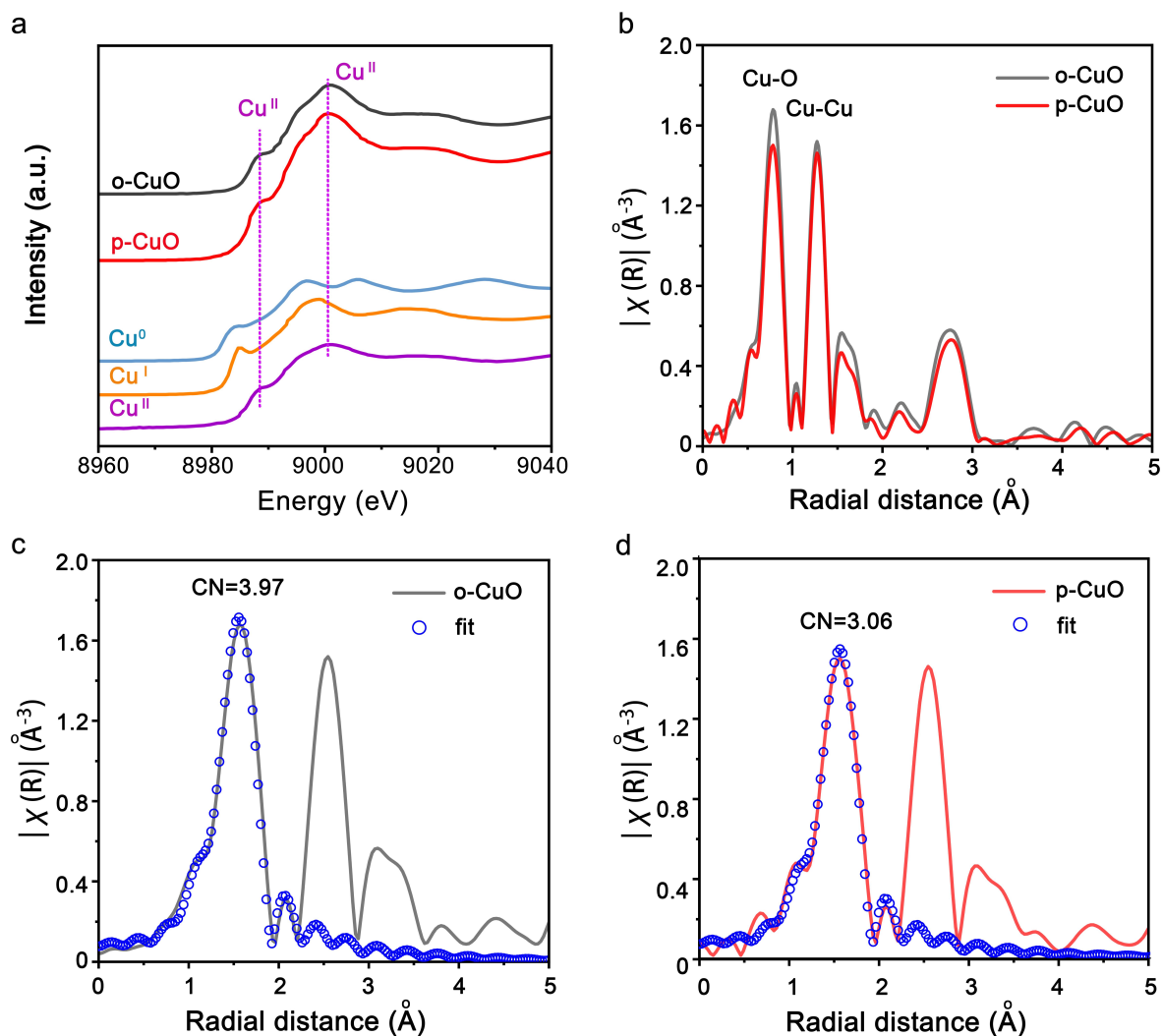
Fig. S10. Structural analyses of o-CuO and p-CuO. (a, b) Cu K-edge XANES spectra (a) and corresponding Fourier transforms of k^3-weighted EXAFS spectra (b) for o-CuO and p-CuO, purchased commercial Cu foil, Cu_2O nanoparticles and CuO nanoparticles reference. (c, d) The average coordination numbers (CN) in the first coordination shell of Cu-O for freshly synthesized o-CuO (c), p-CuO (d) by EXAFS spectra curve fitting. The CN of o-CuO was 3.97; The CN of p-CuO was 3.06. This proved the presence of defective oxygen in p-CuO. (3)
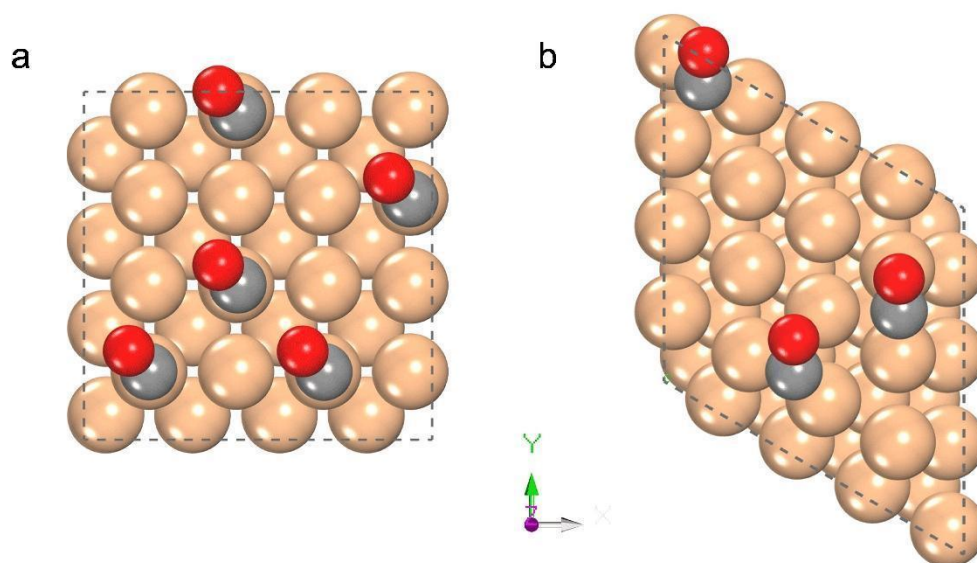
Fig. S11. Calculation models of surface energy. (a) Atop-bound CO intermediates were formed on Cu(100) facets. (b) Bridge-bound CO intermediates were formed on Cu(111) facets. The *CO coverage of Cu (100) was higher than that of Cu (111).
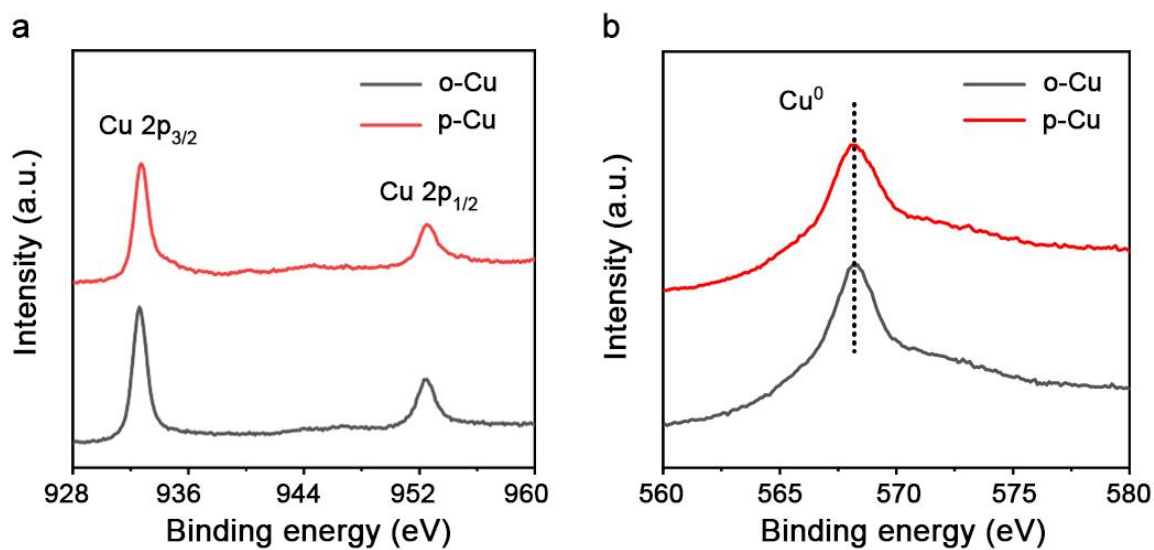
Fig. S12. XPS characterization of o-Cu and p-Cu catalysts. (a) The Cu 2p XPS spectra for o-Cu and p-Cu. The typical peaks at 932.6 and 952.5 eV correspond to the Cu $2P_{3/2}$ and Cu $2P_{1/2}$ of Cu^0/Cu^+, respectively. (b) Cu LMM spectra for o-Cu and p-Cu. The typical peaks at 568.1 eV correspond to the Cu^0. (4) This result confirmed that the valence states of o-Cu and p-Cu were both Cu(0), did not have oxygen vacancy structure.
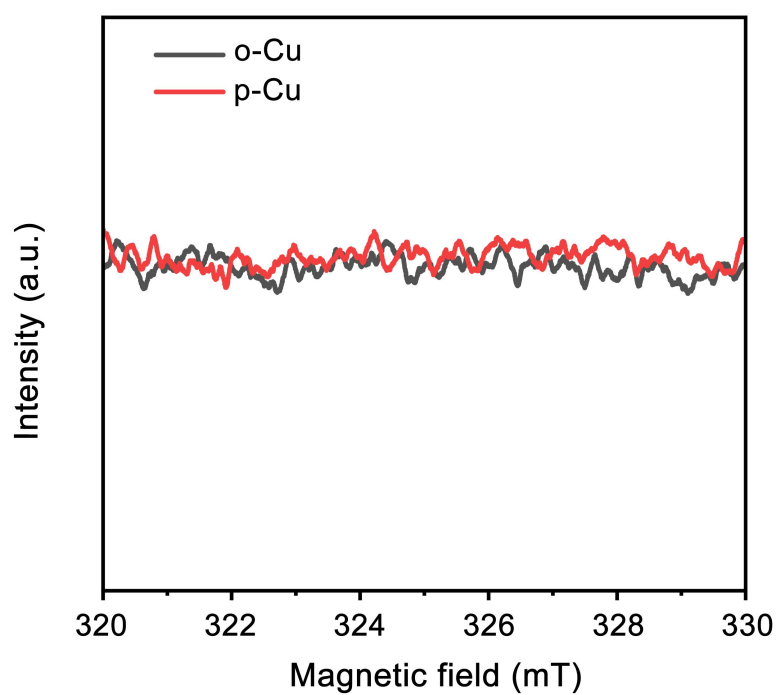
Fig. S13. EPR spectra of the o-Cu and p-Cu catalysts. There was no characteristic waveform represented the formation of oxygen vacancies. This result confirmed that the o-Cu and p-Cu catalysts did not have oxygen vacancy.
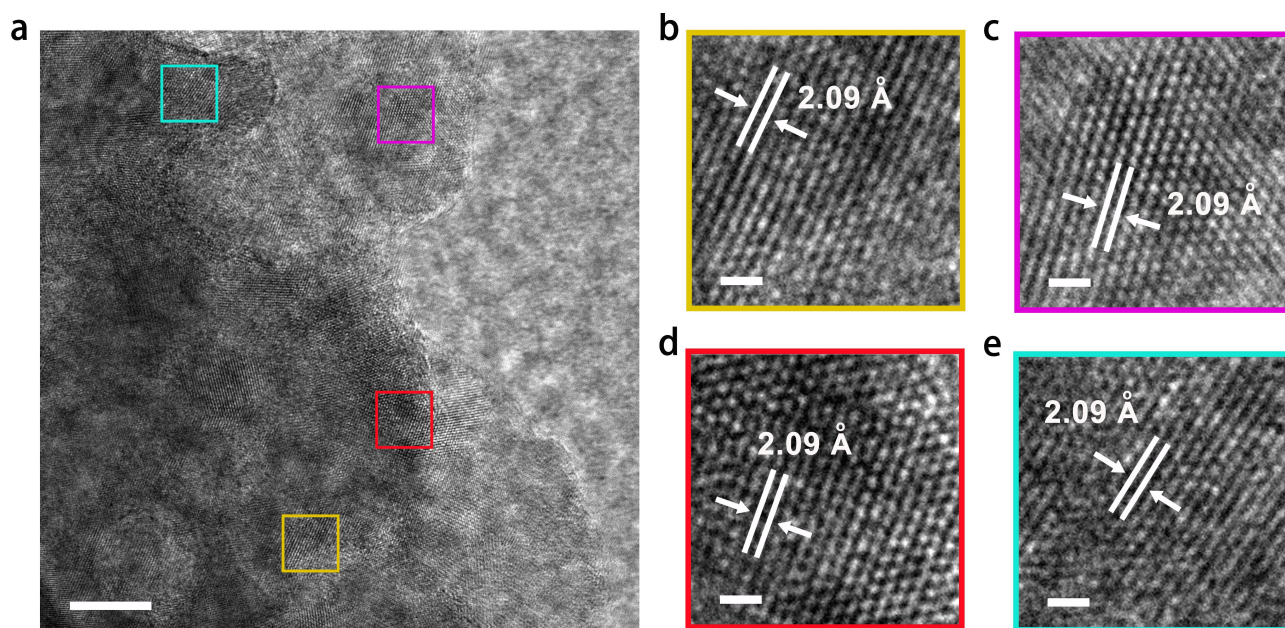
Fig. S14. Structural characterization of o-Cu catalyst. (a) HRTEM image of p-Cu. (b-e) Partially enlarged HRTEM image in the squares of (a). They were taken from randomly-selected spots. Scale bars, (a) 5 nm; (b-d) 0.5 nm. The results showed that the exposed dominant crystal facet on o-Cu was Cu(111).
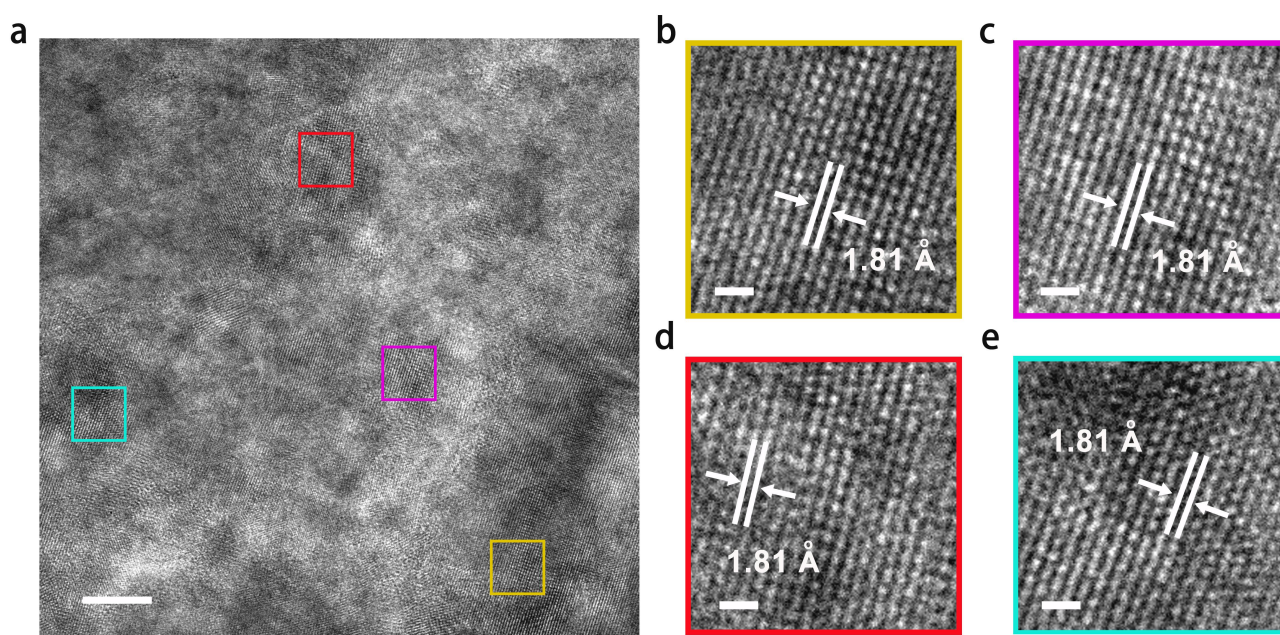
Fig. S15. Structural characterization of p-Cu catalyst. (a) HRTEM image of p-Cu. (b-e) Partially enlarged HRTEM image in the squares of (a). They were taken from randomly-selected spots. Scale bars, (a) 5 nm; (b-d) 0.5 nm. The results showed that the exposed dominant crystal facet on p-Cu was Cu(100).
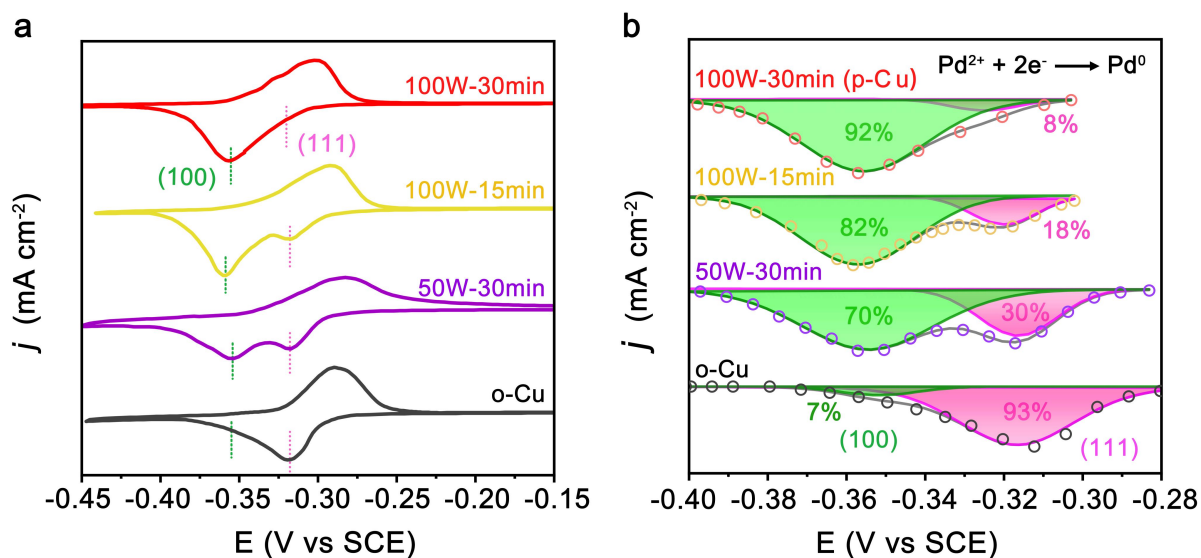
Fig. S16. Surface analysis of the o-Cu and p-Cu catalysts. (a) CV curves of o-Cu (black), 50W-30min p-Cu (purple), 100W-15min p-Cu (blondish) and 100W-30min p-Cu (red) in 2 mM $PbClO_4$ + 0.1 M $KClO_4$ + 1 mM NaCl (pH = 3) aqueous solution. (b) Fitted Pb underpotential deposition (UPD) peaks of o-Cu, 50W-30min p-Cu, 100W-15min p-Cu and 100W-30min p-Cu. The surface features of these catalysts were probed by lead underpotential deposition (Pb^{2+} +2e$^-$ → Pb^0), which yields two reduction peaks at −0.36 and −0.32 V versus SCE for the o-Cu and p-Cu catalysts, suggesting the coexistence of Cu(100) and Cu(111) facets. (5) With the increase of plasma treatment power and time, the proportions of Cu(100) facet of the obtained Cu after reduction increased gradually.
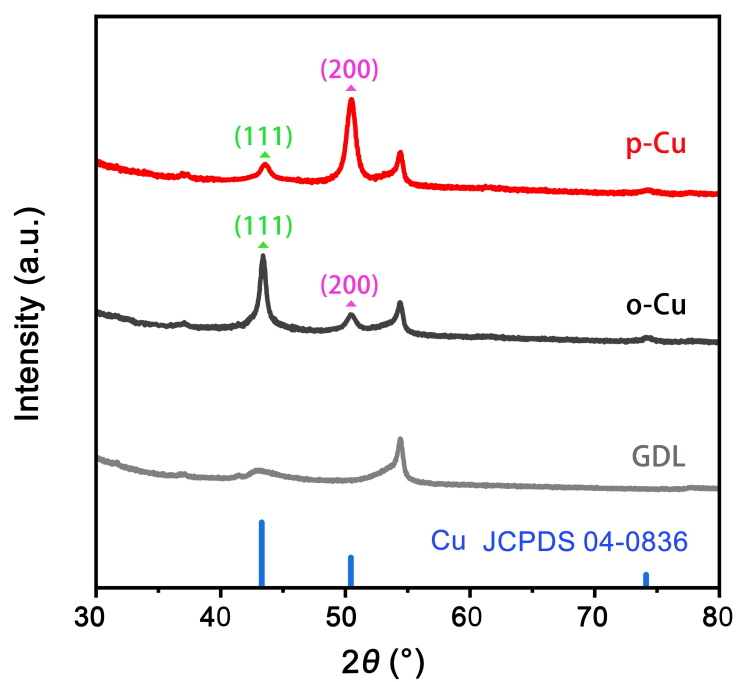
Fig. S17. XRD characterization o-Cu and p-Cu catalysts. It showed that only Cu phase can be detected after pre-reduction. The dominant facets were Cu(111) on o-Cu and Cu(100) on p-Cu.
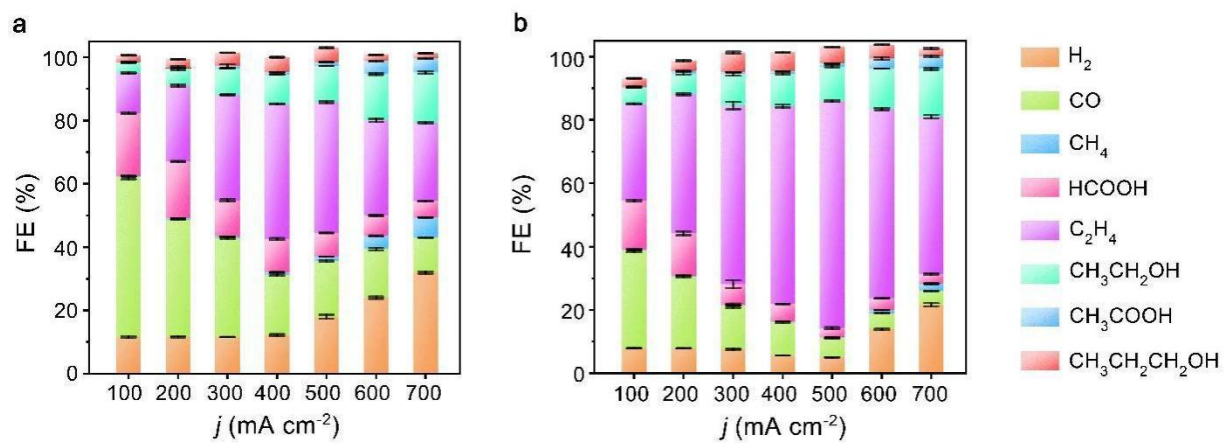
Fig. S18. CO$_2$R performance on different electrodes in a flow cell. (a) o-Cu. (b) p-Cu. Error bars are based on the standard deviation of three independent measurements.
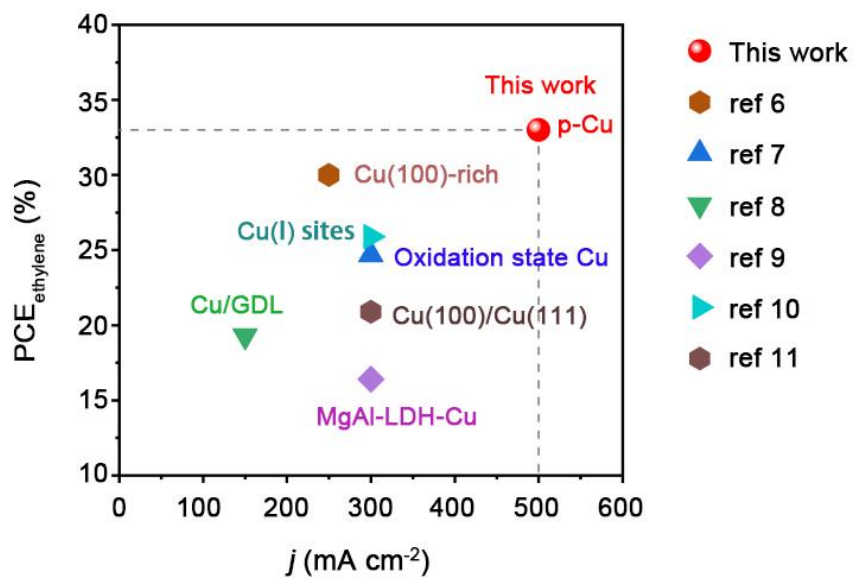
Fig. S19. CO₂R performance. The half-cell PCE for CO$_2$-to-C$_2$H$_4$ conversion on p-Cu. Comparison of the half-cell PCE for various Cu electrodes (operated in neutral electrolytes) reported in the literature. (6-11)
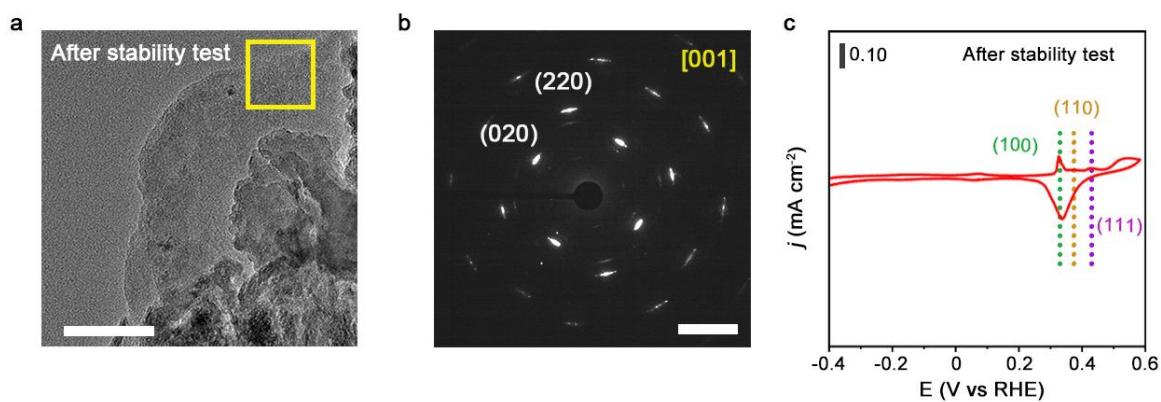
Fig. S20. Structure characterization and surface analysis of p-Cu after stability test. (a) TEM image of p-Cu. Scale bars, 50 nm. (b) The corresponding SAED patterns of a, indicated the electron beams parallel to [001]. Scale bars, 5 1/nm. (c) The CV curves of p-Cu after stability test in 1 M KOH. Scan rate: 20 mV s^{-1}.
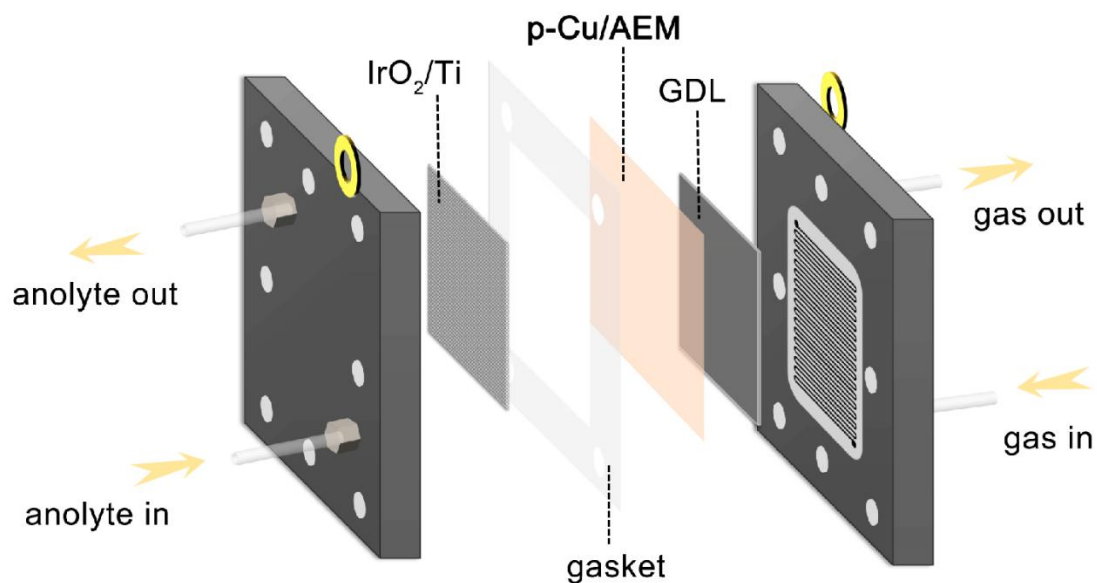
Fig. S21. Schematic of the MEA electrolyser set-up. The MEA electrolyser consists of modules with 2.25 ×2.25 cm^2 opening window. Gaskets are used to seal the reactor. Gas passes through the gas chamber at the back side of the GDE. The electrolytes are circulated between the chambers and collection tank through the silicone tube using a peristaltic pump.
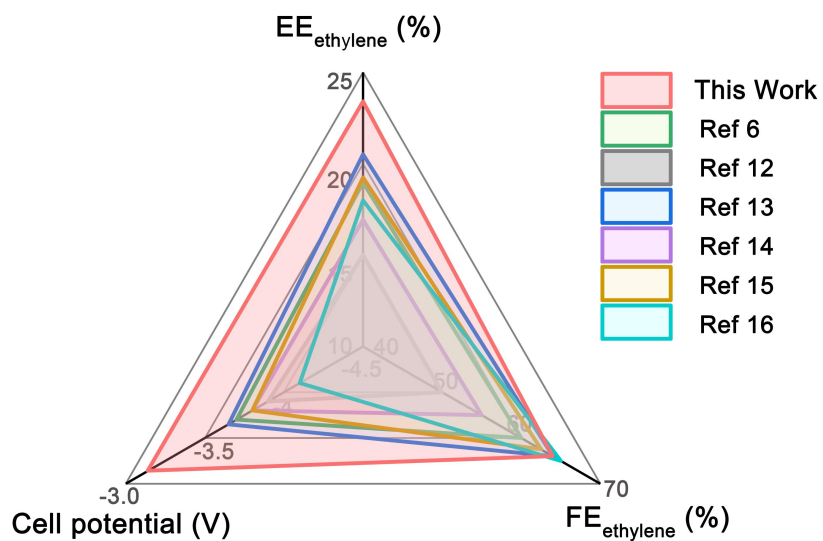
Fig. S22. CO$_2$R performance on p-Cu electrodes in a neutral MEA electrolyser. Comparison of FE of C$_2$H$_4$, energy efficiency of C$_2$H$_4$ and Cell potential for various Cu electrodes reported in the literature. The anode electrolytes were 0.1 M KHCO$_3$. (6, 12-16)
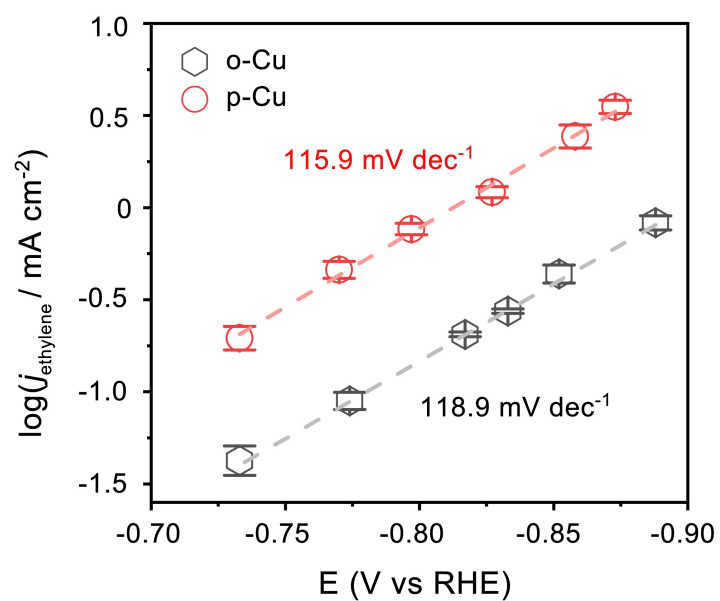
Fig. S23. Tafel curves for COR to C_2H_4. The Tafel slopes of o-Cu and p-Cu were 118.9 mV dec^{-1} and 115.9 mV dec^{-1}, respectively. They were both close to 120 mV dec^{-1}, which indicated that one electron transfer may be involved in the rate-determining step on o-Cu and p-Cu.
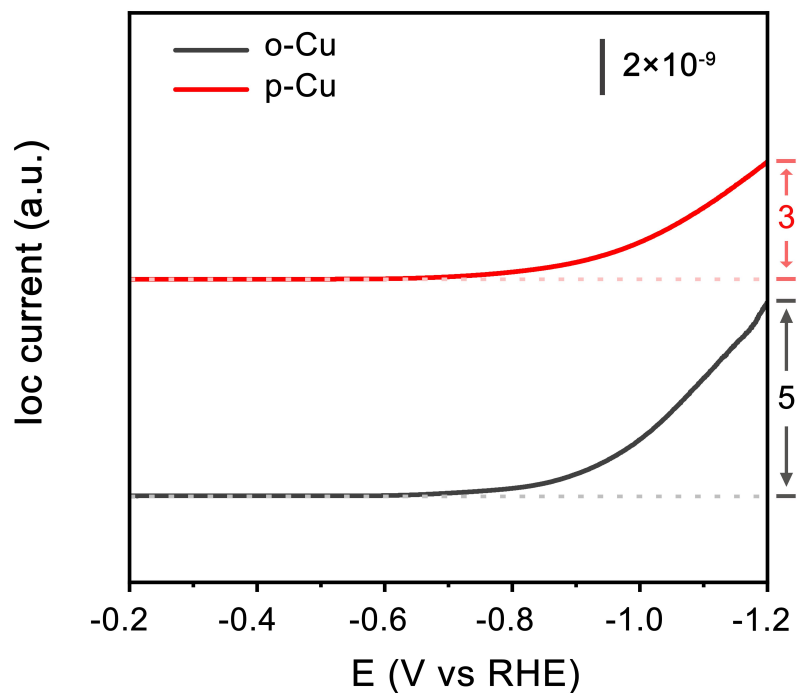
Fig. S24. In situ DEMS data. Mass signals of H_2 (*m/z* = 2) during the cyclic voltammograms test of CO_2R. When the applied potentials were lower than -0.7 V, the signal strength on o-Cu was significantly higher than p-Cu under the same potential conditions. It revealed that o-Cu had higher HER reactivity.
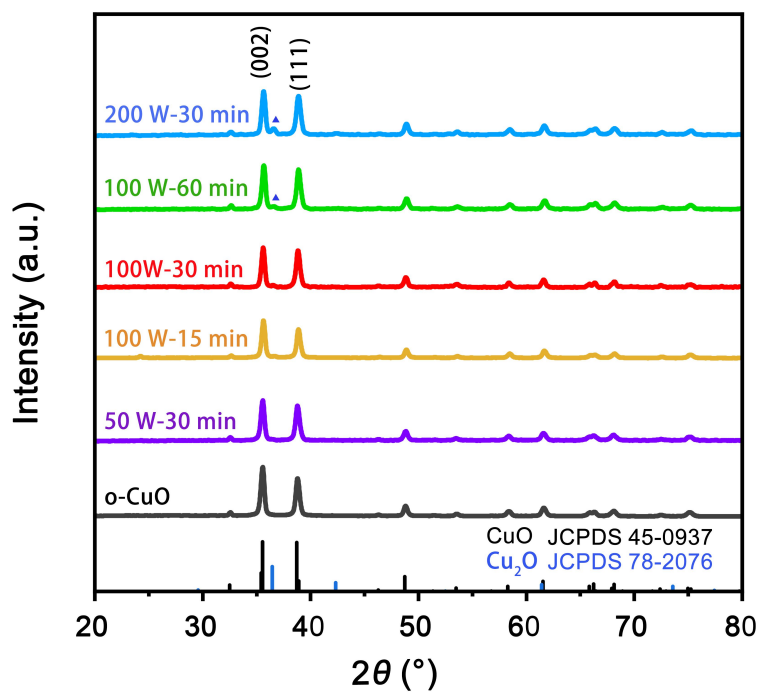
Fig. S25. XRD characterization on different catalysts. XRD pattern of the different catalysts. With the increase of N_2 plasma processing time and power, $Cu_2O(111)$ signal peaks are gradually emerged on CuO nanosheets.
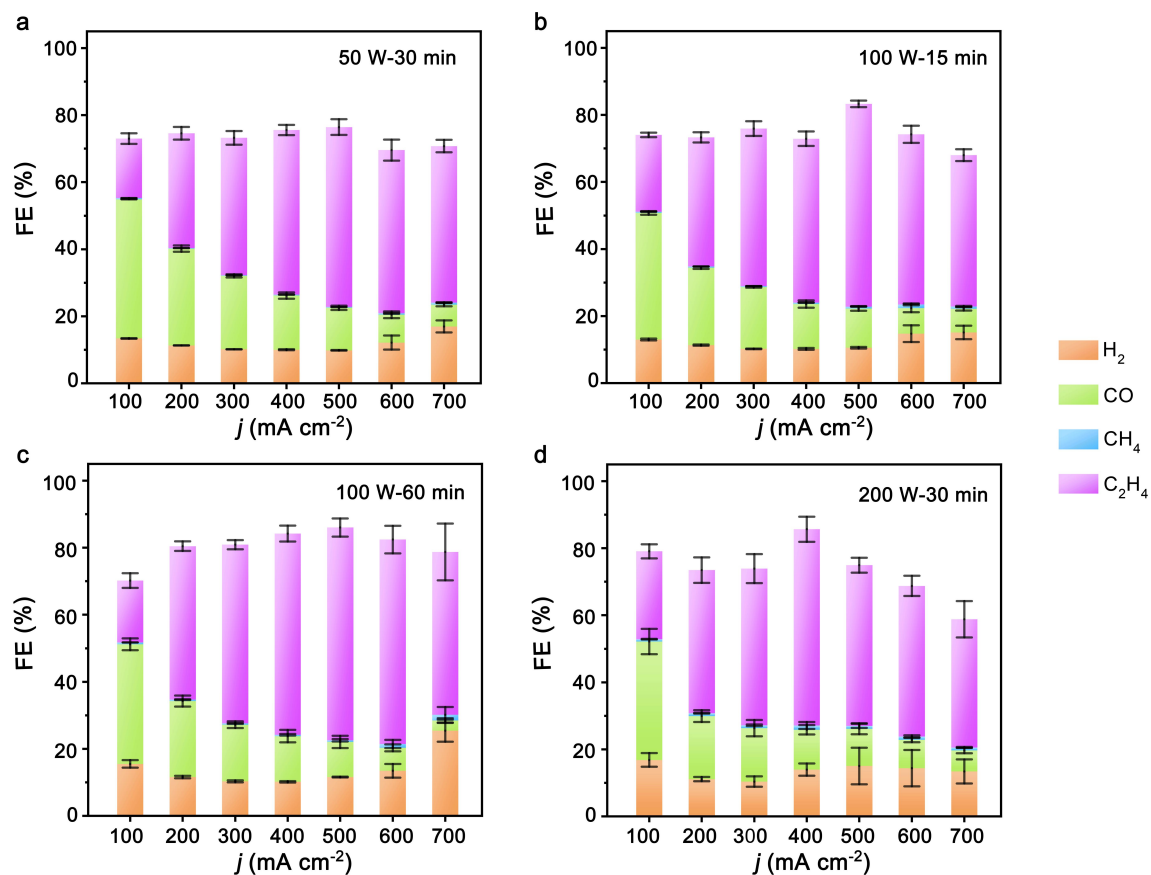
Fig. S26. CO_2R vapor phase products performance on different electrodes in a flow cell. (a) p-Cu electrodes synthesized by N_2 plasma treatment with power of 50 W and reaction time of 30 min. (b, c) p-Cu electrodes synthesized by N_2 plasma treatment with power of 100 W and reaction time of 15 min (b) and 60 min (c), respectively. (d) p-Cu electrodes synthesized by N_2 plasma treatment with power of 200 W and reaction time of 30 min. Error bars are based on the standard deviation of three independent measurements.
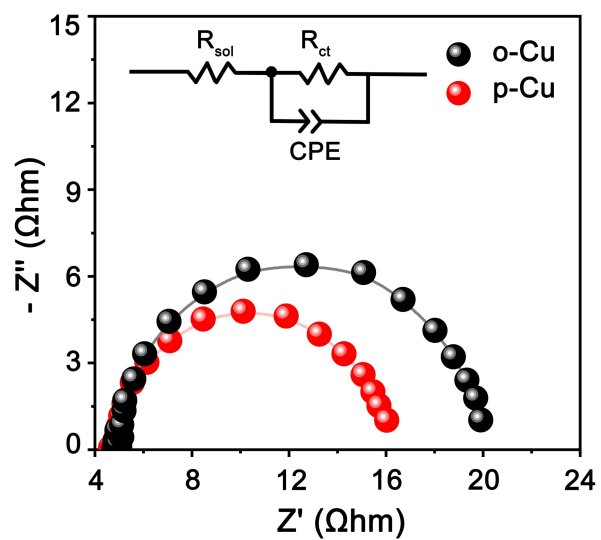
Fig. S27. EIS Nyquist plots. o-Cu and p-Cu had similar solution resistances (R_{sol}) of ~4.8 ohms. And the charge transfer resistances (R_{ct}) were ~15.1, 11.2 ohms for o-Cu and p-Cu, respectively.

Table S1. Average Faraday efficiency data of o-Cu electrodes for CO_2R in a flow cell.

E (V vs RHE)	j (mA cm^{-2})	H$_2$ (%)	CO (%)	CH$_4$ (%)	HCOOH (%)	C$_2$H$_4$ (%)	CH$_3$CH$_2$OH (%)	CH$_3$COOH (%)	CH$_3$CH$_2$CH$_2$OH (%)	C2+ (%)	Total (%)
-1.01	-100	11.59	50.49	0.24	19.96	12.73	3.43	0.03	2.12	18.31	100.59
-1.19	-200	11.66	37.03	0.36	18.03	24.02	5.42	0.02	2.83	32.28	99.37
-1.28	-300	11.60	31.30	0.51	11.33	33.40	8.33	0.74	4.25	46.73	101.47
-1.36	-400	12.24	19.04	0.81	10.49	42.66	9.29	0.70	4.77	57.42	100.01
-1.41	-500	18.00	17.62	1.36	7.48	41.43	11.40	1.18	4.52	58.54	103.00
-1.47	-600	24.00	15.37	4.20	6.40	30.14	14.53	4.12	2.03	50.81	100.78
-1.51	-700	32.00	10.96	6.45	5.13	24.79	15.86	4.43	1.64	46.72	101.25

Table S2. Average Faraday efficiency data of p-Cu electrodes for CO_2R in a flow cell.

E (V vs RHE)	j (mA cm^{-2})	H$_2$ (%)	CO (%)	CH$_4$ (%)	HCOOH (%)	C$_2$H$_4$ (%)	CH$_3$CH$_2$OH (%)	CH$_3$COOH (%)	CH$_3$CH$_2$CH$_2$OH (%)	C2+ (%)	Total (%)
-0.96	-100	7.91	30.86	0.15	15.57	30.57	5.20	0.24	2.64	38.66	93.14
-1.06	-200	7.87	22.73	0.19	13.37	43.94	6.63	0.73	3.26	54.56	98.72
-1.14	-300	7.55	13.78	0.21	6.60	56.38	10.04	0.52	6.16	73.10	101.24
-1.21	-400	5.64	10.56	0.25	5.45	62.53	10.24	0.65	6.05	79.47	101.37
-1.28	-500	5.02	6.07	0.25	2.92	71.69	10.98	0.88	5.23	88.77	103.03
-1.34	-600	13.87	5.15	0.98	3.70	59.78	12.77	3.12	4.42	80.09	103.79
-1.38	-700	21.67	4.31	2.29	3.11	49.69	15.08	3.92	2.46	71.15	102.54

Table S3. Summary of the parameters and CO_2R performances over various Cu catalysts in a flow cell reported previously.

Reactor	Catalyst	Electrolyte	FE$_{ethylene}$ (%)	j$_{ethylene}$ (mA cm^{-2})	Stability(h)	Reference
Flow cell	Cu/PTFE	0.5 M K$_2$SO$_4$	70	350	50	*J. Am. Chem. Soc. 2023, 145, 11, 6339–6348*
Flow cell	MgAl-LDH/Cu	1 M KHCO$_3$	55	168	8	*Angew. Chem. Int. Ed. 2023, 62, e202217296*
Flow cell	SOD/NC-Cu NPs	0.5 M KHCO$_3$	62.5	100	17	*Angew. Chem.Int. Ed. 2023, 62, e202215406*
Flow cell	Cu/GDL	2 M KCl	42	100	30	*J. Am. Chem. Soc. 2021, 143, 3245−3255*
Flow cell	Cu0.9Zn0.1	0.75 M KOH	73	110	150	*Nat. Commun. 2023, 14, 1298*
Flow cell	SHKUST-1	1 M KOH	57.2	229	8	*Angew. Chem. Int. Ed. 2022, 61, e202111700*
Flow cell	Cu-HDD	1 M KOH	58.4	292	16	*Smart Mat. 2022, 3, 194–205*
Flow cell	Cu CIPH	7 M KOH	69	350	No	*Science 2020, 367, 661-666*
Flow cell	Cu-P1	1 M KOH	72	312	3	*Nat. Catal. 2021, 4, 20-27*
Flow cell	p-Cu	1 M KCl	72	359	104	This work

Table S4. Average Faraday efficiency data of p-Cu electrodes for CO_2R in a MEA electrolyser (The anode electrolytes were 0.1 M $KHCO_3$).

E (V)	j (mA cm^{-2})	H$_2$ (%)	CO(%)	C$_2$H$_4$ (%)
-2.46	-40	19.95	12.82	22.51
-2.75	-80	19.41	6.08	36.80
-2.97	-120	17.66	3.84	53.07
-3.14	-160	16.60	2.16	63.84
-3.22	-200	22.98	1.11	46.19

Table S5. Summary of the parameters of different Cu catalysts and the performance of CO_2R in a neutral MEA electrolyser were reviewed reported previously.

Reactor	Catalyst	Electrolyte	$FE_{ethylene}$(%)	Full cell vlotage (V)	$EE_{ethylene}$(%)	Reference
MEA	Sputtering Cu	0.1 M $KHCO_3$	50	3.9	15.0	*Joule 2019, 3, 2777-2791*
MEA	Cu/N-arylpyridinium	0.1 M $KHCO_3$	64	3.65	20.5	*Nature 2020, 577, 509-513*
MEA	Cu(100)-rich catalyst	0.15 M $KHCO_3$	60	3.7	19.0	*Nat.Catal. 2020, 3, 98-106*
MEA	CuNP/Cu	0.1 M $KHCO_3$	55	3.8	16.9	*ACS Energy Lett. 2021, 6, 809-815*
MEA	Carbon shell-coated Cu	0.1 M $KHCO_3$	62.5	3.8	16.9	*Nat.Commun. 2021, 12, 3765*
MEA	Cu-SiOx	0.1 $MKHCO_3$	65	4.1	18.0	*Nat.Commun. 2021, 12, 2808*
MEA	p-Cu	0.1 M $KHCO_3$	64	3.14	23.4	This work

Table S6. The CO reaction order data of o-Cu electrodes for COR at -1.0 V versus RHE.

P_{CO}(atm)	$\log(P_{CO}$/atm)	j (mA cm^{-2})	$FE_{ethylene}$ (%)	$j_{ethylene}$ (mA cm^{-2})	$\log(j_{ethylene}$/mA cm^{-2})
0.10	-1.00	11.50	3.68	0.42	-0.37
0.10	-1.00	12.00	3.41	0.41	-0.39
0.10	-1.00	12.50	3.54	0.44	-0.35
0.20	-0.70	12.60	8.18	1.03	0.01
0.20	-0.70	11.50	7.37	0.85	-0.07
0.20	-0.70	13.80	6.72	0.93	-0.03
0.40	-0.40	16.20	10.99	1.78	0.25
0.40	-0.40	15.30	11.49	1.76	0.25
0.40	-0.40	15.50	14.35	2.22	0.35
0.60	-0.22	17.10	15.93	2.72	0.44
0.60	-0.22	17.20	14.02	2.41	0.38
0.60	-0.22	16.80	17.73	2.98	0.47
0.80	-0.10	19.60	17.70	3.47	0.54
0.80	-0.10	23.60	14.50	3.42	0.53
0.80	-0.10	20.70	13.76	2.85	0.45
1.00	0.00	18.70	17.59	3.29	0.52
1.00	0.00	23.40	15.04	3.52	0.55
1.00	0.00	22.00	13.86	3.05	0.48

Table S7. The CO reaction order data of p-Cu electrodes for COR at -1.0 V versus RHE.

P_{CO}(atm)	log(P_{CO}/atm)	j (mA cm^{-2})	FE$_{ethylene}$ (%)	j$_{ethylene}$ (mA cm^{-2})	log(j$_{ethylene}$/mA cm^{-2})
0.10	-1.00	7.70	4.43	0.34	-0.47
0.10	-1.00	8.34	4.51	0.38	-0.42
0.10	-1.00	7.10	4.89	0.35	-0.46
0.20	-0.70	12.50	12.22	1.53	0.18
0.20	-0.70	10.86	14.07	1.53	0.18
0.20	-0.70	11.30	11.11	1.26	0.10
0.40	-0.40	21.00	26.74	5.61	0.75
0.40	-0.40	20.30	25.20	5.12	0.71
0.40	-0.40	21.30	27.08	5.77	0.76
0.60	-0.22	28.00	36.71	10.28	1.01
0.60	-0.22	30.00	32.43	9.73	0.99
0.60	-0.22	32.00	34.38	11.00	1.04
0.80	-0.10	33.50	35.15	11.78	1.07
0.80	-0.10	26.50	39.76	10.54	1.02
0.80	-0.10	30.00	39.22	11.77	1.07
1.00	0.00	36.00	31.37	11.29	1.05
1.00	0.00	34.00	32.40	11.02	1.04
1.00	0.00	35.50	35.87	12.74	1.11

Table S8. The Tafel slope data of o-Cu electrodes for COR. (CO gas flow rate was 100 mL min^{-1})

E (V vs RHE)	j (mA cm^{-2})	FE$_{ethylene}$ (%)	j$_{ethylene}$ (mA cm^{-2})	log(j$_{ethylene}$/mA cm^{-2})
-0.731	12.5	0.30	0.04	-1.429
-0.730	12.8	0.30	0.04	-1.410
-0.728	13.2	0.40	0.05	-1.282
-0.772	14.3	0.62	0.09	-1.053
-0.769	14.9	0.67	0.10	-1.001
-0.768	15.1	0.53	0.08	-1.094
-0.811	16.5	1.28	0.21	-0.676
-0.811	16.9	1.20	0.20	-0.693
-0.808	17.3	1.17	0.20	-0.695
-0.832	21.5	1.32	0.28	-0.549
-0.836	20.6	1.30	0.27	-0.572
-0.833	21.2	1.28	0.27	-0.566
-0.856	22.5	2.26	0.51	-0.293
-0.854	22.9	1.92	0.44	-0.356
-0.853	23.2	1.68	0.39	-0.409
-0.884	25.2	3.58	0.90	-0.045
-0.886	24.8	3.41	0.84	-0.073
-0.881	25.9	2.90	0.75	-0.125

Table S9. The Tafel slope data of p-Cu electrodes for COR. (CO gas flow rate was 100 mL min^{-1})

E (V vs RHE)	j (mA cm^{-2})	$FE_{ethylene}$ (%)	$j_{ethylene}$ (mA cm^{-2})	log($j_{ethylene}$/mA cm^{-2})
-0.739	10.49	1.90	0.20	-0.701
-0.732	11.86	1.42	0.17	-0.775
-0.724	13.40	1.68	0.22	-0.648
-0.772	15.60	3.29	0.51	-0.289
-0.778	14.45	2.89	0.42	-0.379
-0.766	16.83	2.68	0.45	-0.346
-0.802	19.56	3.99	0.78	-0.107
-0.798	20.30	3.48	0.71	-0.151
-0.794	21.07	3.85	0.81	-0.091
-0.828	24.20	5.43	1.31	0.118
-0.824	24.89	4.75	1.18	0.073
-0.831	23.53	4.89	1.15	0.061
-0.866	36.00	5.91	2.13	0.328
-0.849	42.20	6.69	2.82	0.451
-0.859	37.30	6.46	2.41	0.382
-0.879	41.20	8.34	3.44	0.536
-0.861	44.70	8.66	3.87	0.588
-0.874	42.20	7.85	3.31	0.520

Table S10. The KIE of H/D data of o-Cu electrodes for COR at -1.0 V versus RHE.

H$_2$O as solvent			D$_2$O as solvent			
j (mA cm^{-2})	FE$_{ethylene}$ (%)	j$_{ethylene}$ (mA cm^{-2})	j (mA cm^{-2})	FE$_{ethylene}$ (%)	j$_{ethylene}$ (mA cm^{-2})	KIE
83.5	10.3	8.6	58	7.9	4.6	1.877
80.6	10.4	8.4	63.2	7.2	4.6	1.847
81.2	10.7	8.7	60.5	7.8	4.7	1.843

Table S11. The KIE of H/D data of p-Cu electrodes for COR at -1.0 V versus RHE.

H$_2$O as solvent			D$_2$O as solvent			
j (mA cm^{-2})	FE$_{ethylene}$ (%)	j$_{ethylene}$ (mA cm^{-2})	j (mA cm^{-2})	FE$_{ethylene}$ (%)	j$_{ethylene}$ (mA cm^{-2})	KIE
120	38.3	46.0	105	38.9	40.9	1.125
116	39.0	45.2	100	39.4	39.4	1.149
119	40.0	47.6	102	40.7	41.5	1.147

SI References

1. W. Liu *et al.*, Electrochemical CO(2) reduction to ethylene by ultrathin CuO nanoplate arrays. *Nat. Commun.* **13**, 1877 (2022).
2. N. Zhang *et al.*, Oxide Defect Engineering Enables to Couple Solar Energy into Oxygen Activation. *J. Am. Chem. Soc.* **138**, 8928-8935 (2016).
3. S. Zhao *et al.*, Structural transformation of highly active metal–organic framework electrocatalysts during the oxygen evolution reaction. *Nat. Energy* **5**, 881-890 (2020).
4. M. He *et al.*, Aqueous pulsed electrochemistry promotes C−N bond formation via a one-pot cascade approach. *Nat. Commun.* **14**, 5088 (2023).
5. P. Sebastián-Pascual *et al.*, Surface characterization of copper electrocatalysts by lead underpotential deposition. *J. Electroanal. Chem.* **896**, 115446 (2021).
6. Y. Wang *et al.*, Catalyst synthesis under CO(2) electroreduction favours faceting and promotes renewable fuels electrosynthesis. *Nat. Catal.* **3**, 98-106 (2019).
7. P. P. Yang *et al.*, Protecting Copper Oxidation State via Intermediate Confinement for Selective CO(2) Electroreduction to C(2+) Fuels. *J. Am. Chem. Soc.* **142**, 6400-6408 (2020).
8. X. Zhang *et al.*, Selective and High Current CO(2) Electro-Reduction to Multicarbon Products in Near-Neutral KCl Electrolytes. *J. Am. Chem. Soc.* **143**, 3245-3255 (2021).
9. Y. N. Xu *et al.*, Tuning the Microenvironment in Monolayer MgAl Layered Double Hydroxide for CO_2−to−Ethylene Electrocatalysis in Neutral Media. *Angew. Chem. Int. Ed.* **62**, e202217296 (2023).
10. P. P. Yang *et al.*, Highly Enhanced Chloride Adsorption Mediates Efficient Neutral CO(2) Electroreduction over a Dual-Phase Copper Catalyst. *J. Am. Chem. Soc.* **145**, 8714-8725 (2023).
11. Z. Z. Wu *et al.*, Identification of Cu(100)/Cu(111) Interfaces as Superior Active Sites for CO Dimerization During CO(2) Electroreduction. *J. Am. Chem. Soc.* **144**, 259-269 (2022).
12. C. M. Gabardo *et al.*, Continuous Carbon Dioxide Electroreduction to Concentrated Multi-carbon Products Using a Membrane Electrode Assembly. *Joule* **3**, 2777-2791 (2019).
13. F. Li *et al.*, Molecular tuning of CO(2)-to-ethylene conversion. *Nature* **577**, 509-513 (2020).
14. Y. Xu *et al.*, Self-Cleaning CO_2 Reduction Systems: Unsteady Electrochemical Forcing Enables Stability. *ACS Energy Letters* **6**, 809-815 (2021).
15. J. Y. Kim *et al.*, Quasi-graphitic carbon shell-induced Cu confinement promotes electrocatalytic CO(2) reduction toward C(2+) products. *Nat. Commun.* **12**, 3765 (2021).
16. J. Li *et al.*, Silica-copper catalyst interfaces enable carbon-carbon coupling towards ethylene electrosynthesis. *Nat. Commun.* **12**, 2808 (2021).